



Selective photocatalytic oxidation of furfural to C₄ compounds with metal-TS-1 zeolite

Wanying Liang^{a,1}, Guangyue Xu^{a,b,*}, Yao Fu^{a,**}

^a Hefei National Research Center for Physical Sciences at the Microscale, iChEM, CAS Key Laboratory of Urban Pollutant Conversion, Anhui Province Key Laboratory of Biomass Clean Energy, University of Science and Technology of China, Hefei 230026, China

^b Institute of Energy, Hefei Comprehensive National Science Center, Hefei 230031, China

ARTICLE INFO

Keywords:

Biomass resources
C₄ carboxylic acids
Metal-TS-1 zeolite
Photocatalysis

ABSTRACT

A series of metal-TS-1 zeolite catalysts were designed to selectively catalyze the photo oxidation of furfural to C₄ carboxylic acid derivatives at ambient temperature and pressure. The photocatalytic preparation of maleic acid from furfural was realized for the first time. The selective distribution of products could be controlled by adjusting the physical and chemical characteristics of the catalyst. Smaller pore size prevented the further conversion of maleic acid to malic acid; moderate acidity was beneficial for the preparation of maleic acid; lower valence band was in favor of maleic acid production while higher valence band tended to form malic acid. The synergistic effect of pore structure, acidity and energy band structure of catalysts affected the product distribution. The yield of maleic acid reached as high as 40% over Fe-TS-1, meanwhile, the yield of malic acid reached as high as 63% over Ni-TS-1. The doping of metal was believed to be an effective procedure to adjust the structure and physicochemical properties of zeolite. Metal-TS-1 zeolite was also expected to be widely used in photocatalytic system to achieve more selective reactions.

1. Introduction

In response to the rapid depletion of fossil fuels, the quest for alternatives to sustain the production of chemicals and fuels has garnered growing attention [1–3]. Biomass is a promising renewable carbon source that has the potential to be converted on a massive scale into chemical and liquid transport fuels [4–6]. It has been transformed into a variety of platform molecules [7,8]. Among them, furfural, which is produced by the acid hydrolysis of hemicellulose in biomass resources, is a type of platform compound with significant growth potential [9,10]. Furfural has a highly functionalized molecular structure, which can be further converted into numerous fossil fuel substitutes and value-added chemicals with extensive commercial applications. One application path of furfural is to synthesize downstream C₄ chemicals through selective oxidation of furfural, including C₄ carboxylic acids such as maleic acid and malic acid, and intermediate products such as hydroxyfuranone and furanone, as shown in Scheme 1. These value-added chemicals all have a high industrial value. Unfortunately, it is still a problem to selectively

obtain these products.

Maleic acid is one of the necessary C₄ intermediates for the synthesis of unsaturated polyester resins, vinyl copolymers, surface coatings, and drugs. At present, maleic acid is mainly industrially produced by catalytic oxidation of petroleum-derived raw materials such as butane [11]. However, with the depletion of fossil raw material and the increasing emphasis on green chemistry, production lines using chemicals derived from renewable biomass, such as furfural and maleic acid, are receiving increasing attention. In previous work, the process of preparing maleic acid by selective oxidation of furfural had been widely reported, and most of the work also obtained a high yield of maleic acid by optimizing reaction conditions [12–16]. For example, Granados et al. used liquid phase oxidation system to replace the previous industrial gas phase oxidation system using O₂, avoiding the harsh conditions of high pressure [17]. They mentioned that when H₂O₂ was used as an oxidant, the concentration ratio of H₂O₂ to the substrate furfural had an important effect on the reaction selectivity. Lou et al. discussed the reaction conditions of selective oxidation of furfural to maleic acid in detail [18].

* Corresponding author at: Hefei National Research Center for Physical Sciences at the Microscale, iChEM, CAS Key Laboratory of Urban Pollutant Conversion, Anhui Province Key Laboratory of Biomass Clean Energy, University of Science and Technology of China, Hefei 230026, China.

** Corresponding author.

E-mail addresses: craneyue@mail.ustc.edu.cn (G. Xu), fuyao@ustc.edu.cn (Y. Fu).

¹ These authors contributed equally to this work.

They pointed out that when H_2O_2 was used as oxidant, the oxidation potential in the system could be adjusted by adjusting the pH of the reaction solution to improve the product selectivity. Cao et al. designed carbon-based catalysts modified by highly sulfonated groups to obtain maleic acid from furfural with high selectivity. They suggested that the Lewis acidic site on the catalyst surface was the key to improve the reaction selectivity [19]. To date, as mentioned in their work, few heterogeneous catalytic systems had been developed for the oxidation of furfural to maleic acid. Metal-containing catalysts had a problem with metal leaching, whereas metal-free catalysts had insufficient catalytic activity. Researches on heterogeneous catalysts still had many limitations. In addition, almost all research systems were limited to high-temperature or liquid acid/ base assistance [20,21].

Malic acid can be obtained by further hydration reaction of maleic acid. Maleic acid, which can be used to treat a variety of ailments, is a crucial key chemical intermediate in the food and pharmaceutical sectors. Maleic acid is mostly obtained by biological fermentation. In addition, maleic acid can also be obtained by the hydration reaction of maleic acid under high temperature and pressure. At present, barely any effective synthesis of malic acid by chemical synthesis has been reported. Maleic acid has only been found as a trace by-product in few works [22,23]. The direct oxidation of furfural to malic acid has not been reported at present. But there is no denying that, this possible path is worth exploring.

In addition, the oxidation of furfural is often accompanied by the formation of 5-hydroxy-2,5(H)-furanone (HFU), which is an intermediate product of the oxidation of furfural to maleic acid [24]. HFU exists widely in natural products and drug structures, and is the basic raw material for synthesizing a series of chiral compounds with physiological activity. The preparation of HFU using furfural as substrate has been widely reported [25–27]. Among them, the preparation of HFU by photosensitive oxidation has been deeply studied. Compared with the catalytic oxidation of furfural to prepare HFU at high temperature liquid phase, photocatalytic oxidation has the advantages of mild reaction conditions, easy to control, high yield, and environmental friendliness. However, the photosensitizer itself also has the unavoidable disadvantage of unrecyclable, which severely limits its photocatalytic application process [28–30].

Titanium Silicate-1 (TS-1) zeolite was widely used as heterogenous photocatalyst. It has large specific surface area, abundant microporous structure, and high stability. It performs excellently as a photocatalyst due to its strong light transmission properties and high molecular

diffusion coefficient, which facilitates the quick separation of photo-generated electron-hole pairs [31–34]. In addition, the structure of zeolite materials is adjustable, which can in turn change the physicochemical properties of the composite. In recent years, composite zeolite innovative materials have been widely concerned [35].

In this study, we designed a class of metal-TS-1 zeolite composite catalysts. Using TS-1 as skeleton, active metal species were doped into TS-1 skeleton and its related sites by hydrothermal method. Metal-TS-1 zeolite catalysts had the advantages of metal stability, adjustable acidity, and adjustable redox potential. By modifying the catalyst, downstream C_4 chemicals could be selectively obtained by photocatalytic oxidation of furfural. The relations between product selectivity and the physicochemical characteristics of catalysts were further explored.

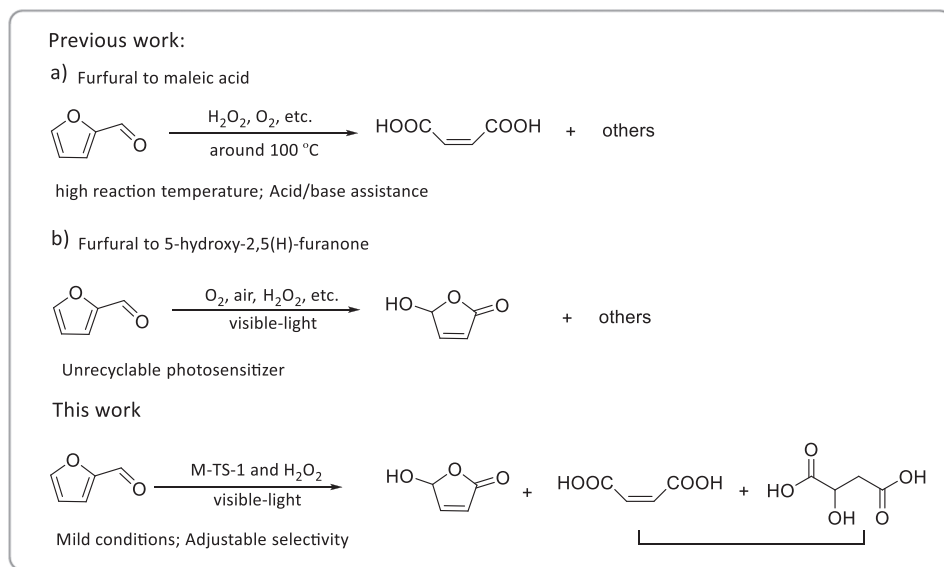
2. Experimental

2.1. Reagents

Tetrapropylammonium hydroxide (TPAOH), Tetraethyl orthosilicate (TEOS), Tetrabutyl titanate, Propan-2-ol, Magnesium nitrate hexahydrate ($\text{Mg}(\text{NO}_3)_2 \cdot 6 \text{H}_2\text{O}$), Aluminium nitrate nonahydrate ($\text{Al}(\text{NO}_3)_3 \cdot 9 \text{H}_2\text{O}$), Nickel nitrate hexahydrate ($\text{Ni}(\text{NO}_3)_2 \cdot 6 \text{H}_2\text{O}$), Iron nitrate nonahydrate ($\text{Fe}(\text{NO}_3)_3 \cdot 9 \text{H}_2\text{O}$), Cobalt nitrate hexahydrate ($\text{Co}(\text{NO}_3)_2 \cdot 6 \text{H}_2\text{O}$), Copper nitrate hydrate ($\text{Cu}(\text{NO}_3)_2 \cdot 3 \text{H}_2\text{O}$), Zinc nitrate hexahydrate ($\text{Zn}(\text{NO}_3)_2 \cdot 6 \text{H}_2\text{O}$), Gallium(III) nitrate hydrate ($\text{Ga}(\text{NO}_3)_3 \cdot x \text{H}_2\text{O}$), Zirconium(IV) nitrate pentahydrate ($\text{Zr}(\text{NO}_3)_4 \cdot 5 \text{H}_2\text{O}$), Ammonium molybdate ($\text{H}_{24}\text{Mo}_7\text{N}_6\text{O}_{24} \cdot 4 \text{H}_2\text{O}$), Indium chloride (InCl_3), Lanthanum chloride (LaCl_3), Bismuth nitrate pentahydrate ($\text{Bi}(\text{NO}_3)_3 \cdot 5 \text{H}_2\text{O}$), Ammonium Metatungstate ($(\text{NH}_4)_6\text{H}_2\text{W}_{12}\text{O}_{40} \cdot x \text{H}_2\text{O}$), Furfural, Maleic acid, Malic acid, Furoic acid, 5-hydroxy-2,5(H)-furanone (HFU), 5-(H)-furanone, Formic acid, Hydrogen peroxide 15%. The above drugs were purchased from Aladdin Chemical Reagent Co., Ltd.

2.2. Catalyst preparation

As a typical run for the synthesis of M-TS-1, 7.5 g of TEOS, 5.81 g of TPAOH solution were mixed with 5.79 g of DI water, followed by sonicating until the solution was clear. 0.32 g of tetra-n-butyl titanate was dissolved in 1.2 g of isopropanol, mixed and added dropwise to the solution. The mixture was stirred continuously for 2 h at 70 °C. A computational amount of metal solutions (Si:M=47:1) was added into



Scheme 1. Catalytic oxidation of furfural.

the precursor solution. The obtained solution was transferred into a 100 mL Teflon-lined stainless steel autoclave and crystallized at 170 °C for 24 h under static conditions. The solid product was then collected by the centrifugation and washed with water several times, and then dried at 80 °C in the oven. Finally, the as-synthesized samples were calcinated in air at 550 °C for 2 h. This class of catalysts was named M-TS-1. The added metals were Mg, Al, Fe, Co, Ni, Cu, Zn, Ga, Zr, Mo, In, La, W and Bi respectively.

2.3. Catalyst test

The photocatalytic system was performed in a 10 mL reaction tube. In a typical oxidation reaction, 0.1 mmol furfural (distilled before use) and 0.6 mmol 15% H₂O₂ were dissolved in 1 mL of water, then 5 mg of the catalyst was added. The photocatalytic system was irradiated under 390 nm light and magnetic stirring. The reaction time of single tube was 10 h. The photocatalytic equipment was shown in Fig. S1-S3. After the reaction was completed, the catalyst was separated by filtration, and the solution was analyzed using a high-performance liquid chromatography (HPLC) system equipped with a Biorad Aminex HPX-87H column and a RID detector. Quantification was performed using commercial standards for calibration. The product was characterized by HPLC-MS, as shown in Fig. S4. Furfural conversion and product yields were calculated using the following equations:

$$\text{Conversion(\%)} = \frac{\text{Moles of feedstock consumed}}{\text{Moles of feedstock input}} \times 100\%$$

$$\text{Product yield(\%)} = \frac{\text{Moles of product}}{\text{Moles of feedstock input}} \times 100\%$$

2.4. Catalyst characterization

The X-ray diffraction patterns (XRD) of the powder samples was detected by the sample level high power X-ray powder diffractometer (TTR-III, Rigaku, Japan), using Cu K α radiation at 40 kV and 15 mA. The 2 θ range was 5–65°, and the step length was 0.02°.

The BET-specific surface area and N₂ adsorption-desorption isotherms of samples were measured at 77 K (Tristar II 3020M, Micromeritics, America). Sample pre-activation procedure: degas at 120 °C for 2 h and then activate at 300 °C for 2 h. The sample weight after activation was 0.1 g. According to the N₂ adsorption/desorption isotherm, the specific surface area and pore size distribution of the catalyst were calculated by BET and BJH methods, respectively.

The FT-IR of the samples was detected by the Fourier transform infrared spectrometer (Nicolet 8700, Thermo Nicolet, America). The sample was mixed with KBr in a certain proportion for testing and analysis.

The Raman of the samples was detected by the Laser Raman spectrometer system (LabRamHR, Jobin Yvon, France).

The UV-vis of the samples were detected by the Ultraviolet-visible-near-infrared spectrophotometer (SOLID3700, Shimadzu, Japan).

The Photoluminescence Spectroscopy (PL) of the samples were detected by the Steady-state/transient fluorescence spectrometer (JY Fluorolog-3-Tou, Jobin Yvon, France).

X-ray photoelectron spectroscopy experiments (XPS) and Ultraviolet photoelectron spectroscopy (UPS) were performed on ESCALAB 250Xi (Thermo Scientific, England) spectrometer. Test conditions: ultimate vacuum of analysis chamber: 5 × 10^{−10} mbar; monochromatic X-ray source: Al K α 150 W, beam spot 500 μ m; Energy resolution and sensitivity: when the FWHM of Ag3d_{5/2} was 0.6 eV, the intensity was greater than 1600,000 cps. The C1s photoelectron peak with a binding energy of 284.8 was used as a reference to correct the spectrum.

TEM of the samples was detected by the Transmission electron microscope (JEM-2011, Electronics Corporation, Japan). EDS mapping was mainly used to observe the microscopic appearance and element

distribution of samples (JEM-2100 Plus, HT7700 Exalens, JEOL Ltd., Japan). Point resolution: 0.23 nm; fringe resolution: 0.14 nm; acceleration voltage: 200 kV; magnification: 30–1.5 × 10⁶; tilt angle: ± 30°; element analysis range: 5B ~ 92U; camera: SIS QUEMESA 11 million pixels Bottom inserted CCD. Sample preparation process: a small amount of catalyst was dispersed in ethanol and spot coated on qualitative filter paper.

NH₃-TPD of the samples was detected by the Fully automatic chemisorption instrument (VDSorb 91i, Quzhou Ward Instrument Co., LTD, China). Standard process: 0.1 g sample with a diameter of 40–60 mesh was filled into the quartz reaction tube, and the two ends were stuffed with quartz cotton to prevent the sample from blowing out and blocking the tube. TCD temperature was set as 80 °C. NH₃/He (1.05%/98.95% by volume) gas flow was 40 sccm. Then the samples were pre-treated in a flowing He atmosphere at 200 °C for 60 min to remove residual moisture and adsorbed impurities on the sample surface. After cooling to 80 °C, He was switched to NH₃ for 60 min to ensure the adsorption capacity of NH₃ reached saturation of the sample. Then the gas path was switched to He to remove the NH₃ physically adsorbed on the surface of the sample. After the NH₃ signal was stable, the temperature was heated up to 500 °C at the heating rate of 10 °C/min. Meanwhile, the desorption signal of NH₃ during the heating process was recorded.

Electrochemical impedance (EIS) and Mottschottky curve (MS) were detected by the Electrochemical workstation (CHI760E, Shanghai Chenhua Instrument Co., LTD, China). The experiment adopted a three-electrode system, with platinum wire as the counter electrode and Ag/AgCl electrode as the reference electrode. The samples were uniformly coated on ITO conductive glass as the working electrode. The electrolyte was 0.2 M Na₂SO₄ solution.

An inductively coupled plasma optical emission spectrometer (ICP-OES, 5110 ICP-OES, RF Power: 1.20 KW) was used to analyze the content of each element in the sample.

Electron paramagnetic resonance (EPR) was used for the direct detection and studying of materials containing unpaired electron paramagnetism. In-situ ESR was processed using JES-FA 200 (JEOL) with sensitivity of 7 × 10⁹ spins/0.1mT.

3. Results and discussion

3.1. Physicochemical property characterizations

Different M-TS-1 catalysts were prepared by doping various metals into TS-1 zeolite. The XRD and TEM of each sample were shown in Fig. 1. Through the XRD pattern, it could see that all the samples showed typical MFI structure characteristic peaks, without anatase-TiO₂ or other metal oxide peaks appearing. As shown in Fig. S5, it could be seen from the mapping that the added metals were uniformly dispersed without obvious agglomeration. It indicated that these catalysts had high crystallinity and there was no or only a very small amount of TiO₂ or other metal oxides in the samples. Fig. 1B showed the TEM morphologies of all samples, which provided that all the samples were roughly ellipsoid like, with lamellar or bulk superposition morphology. As shown in Fig. S6, the metal incorporation had a certain effect on the particle size and overall morphology of zeolite. The particle size of most samples was concentrated in the range of 100–140 nm, and the particles showed uniform bulk morphology. A part of samples such as Fe-TS-1 and Mo-TS-1 were special because they had a morphology of polycrystal and significantly increased particle size (about 200 nm). Similar situation also appeared in Ga-TS-1 and Al-TS-1. The size of the zeolite may affect the mass transfer of the reacting molecules.

To explore the pore structure of the samples, the BET surface area (S_{BET}) and pore size of these catalysts were determined by N₂ adsorption-desorption. Fig. S7 showed the N₂ adsorption-desorption curves of each sample. Almost all the samples showed the combination of type I and type IV isotherms, and the hysteresis ring in the high

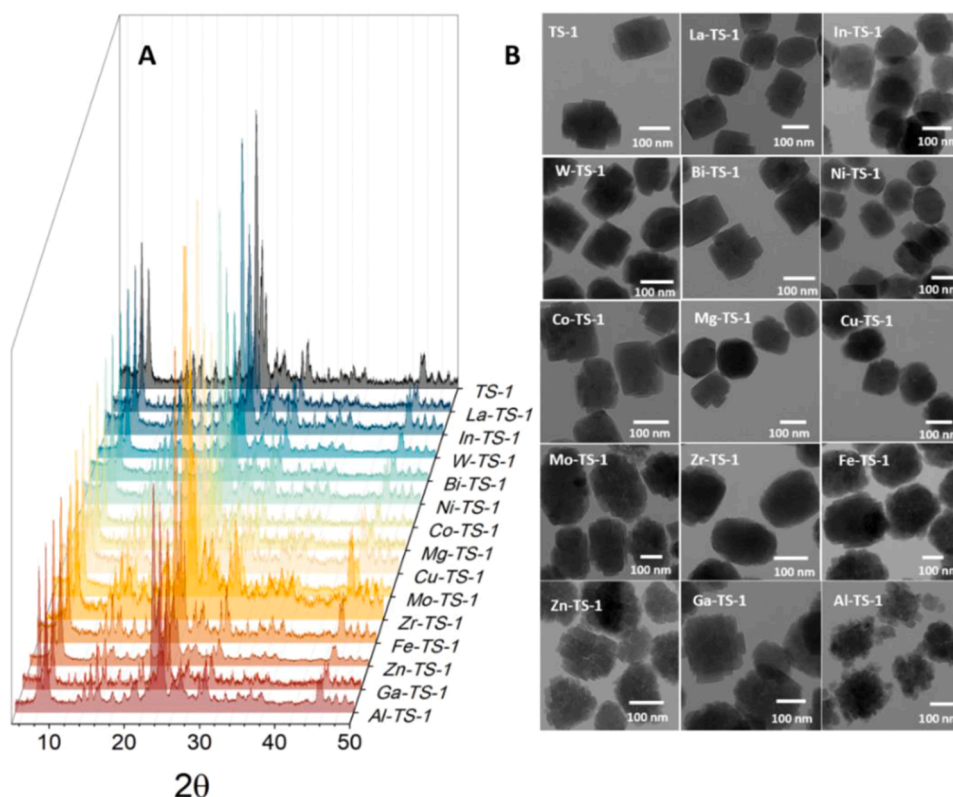
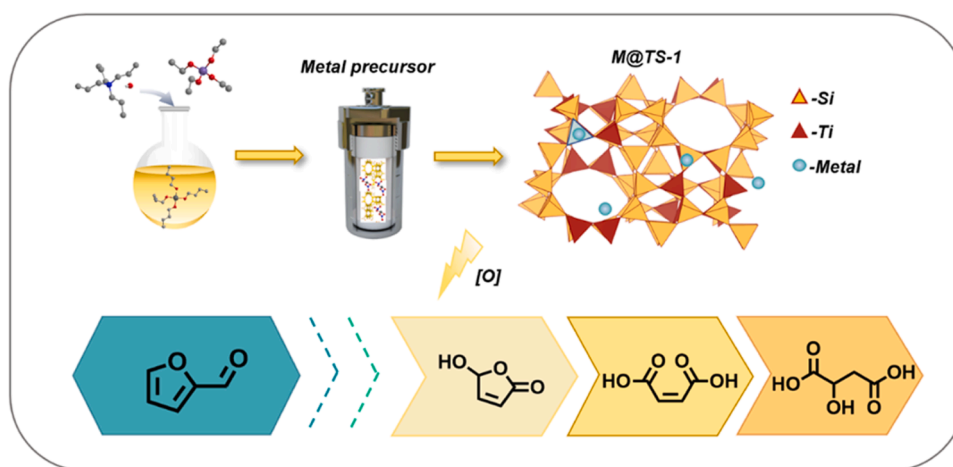


Fig. 1. XRD patterns (A) and TEM images (B) of as-prepared samples.



Scheme 2. The design and preparation process of M-TS-1 catalyst and the downstream product of furfural oxidation.

specific pressure region indicated the existence of mesopore formed by grain accumulation, which was related to the nano-size of the samples [36]. In addition, combined with TEM results, the increase of zeolite particle size was accompanied by the decrease of the degree of intergranular accumulation, showing that the hysteresis rings in the high specific pressure region gradually decreased. In particular, the hysteresis characteristics of Fe-TS-1 and Mo-TS-1 were almost negligible. Fig. S8 showed the BJH pore size distribution of each sample. It could be observed that the results were consistent with the N_2 adsorption-desorption curve, that is, most of samples had mesoporous characteristics. Among them, samples like Fe-TS-1 and Mo-TS-1 were still special for they had obvious pore size at about 4 nm, which were corresponded to TEM results. The pores could be corresponded to intercrystalline mesopore formed by the stacking of grains. Similar

situation also appeared in Ga-TS-1, Al-TS-1 and Zn-TS-1. Table S2 showed the physical and chemical characteristic data of each sample, including specific surface area, pore volume, pore size, etc. Pore volume and pore size had a great influence on the selectivity of reaction products.

The FT-IR spectra of each sample were shown in the Fig. 2. All the samples showed six obvious characteristic absorption peaks between 400 and 1600 cm^{-1} , which were at 450, 550, 800, 960, 1100, and 1225 cm^{-1} , respectively. Among them, the characteristic peaks at 550 cm^{-1} and 1225 cm^{-1} were the characteristic vibration peaks of zeolite with MFI topology. Each sample had typical MFI characteristic vibration peaks. In addition, most researchers attributed the absorption peak at 960 cm^{-1} to the Si-O bond vibration caused by the entry of Ti or other transition metals into the zeolite skeleton [37]. It can be found

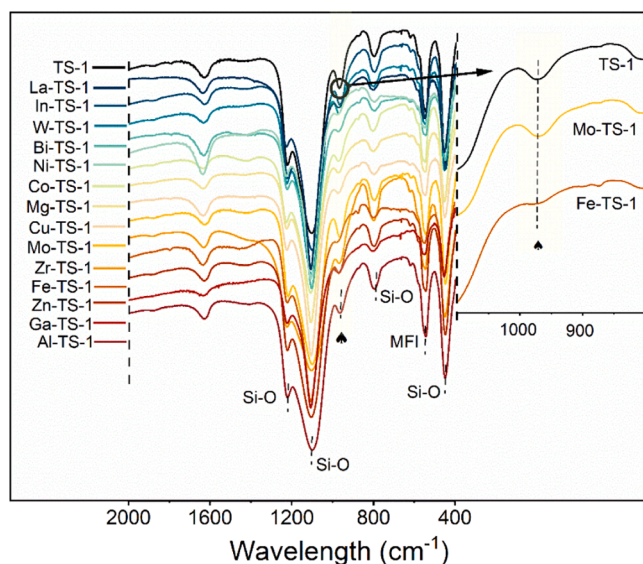


Fig. 2. FT-IR spectra of samples.

from Fig. 2 that for the absorption peak at 960 cm^{-1} , the absorption signal of M-TS-1 after the doping of most metals was similar or stronger than that of TS-1 (such as Mo-TS-1). These results indicated that these metals entered into the zeolite channel or replaced Ti in the skeleton, which caused strong Si-O bond vibration. However, for Fe-TS-1, the signal of absorption peak at 960 cm^{-1} was obviously weakened, suggesting that Fe had a different location in zeolite structure. In other words, Fe replaced the skeleton Si atom and changed the zeolite structure, which weakened the overall Si-O bond vibration.

Fig. 3 showed the UV-Raman spectra of each sample at $\lambda_{\text{ex}} = 325\text{ nm}$. Most of the samples had the same characteristic peak as TS-1, which were attributed to the tetra-coordinate skeleton Ti, "TiO₄" site [38]. Some samples showed anatase-TiO₂ characteristic peaks, such as La-TS-1, Bi-TS-1 and In-TS-1, which was due to the incorporation of these metals affected the crystallization process of M-TS-1. In addition, it could be seen that the characteristic peaks of Fe-TS-1 and Mo-TS-1

varied greatly compared with TS-1. Almost all the characteristic peaks of Ti-O in Mo-TS-1 disappeared, but the characteristic peaks of Si-O remained. This was due to the fact that Mo entered the zeolite skeleton to replace the skeleton Ti atom, which seriously damaged the original crystal structure of TS-1. New characteristic peaks were generated in Fe-TS-1, while all structural characteristic peaks on TS-1 disappeared. This phenomenon was also due to Fe entered the zeolite framework. However, contrary to the behavior of Mo, Fe replaced the skeleton Si atom, which generated a new structure Fe-O-Ti, resulting in a complete change of the original structure. The change of crystal structure and skeleton elements would greatly affect the solid acid content of the samples.

To explore the changes of electron state in surface element before and after the addition of metals, XPS Ti 2p spectra of all samples were compared in the experiment, and the results were shown in Fig. 4A. Ti in bare TS-1 was mostly in the tetra-coordination state. Meanwhile, there was also a few anatase-TiO₂ species, which may be caused by incomplete crystallization. As shown in Table S3, after doping different metals, the content of anatase-TiO₂ in some samples increased significantly, such as Mo-TS-1. These TiO₂ might be dispersed on the zeolite surface, showing increased Ti/Si content on the sample surface. This result was due to the fact that the addition of these metals seriously affected the crystal structure and crystallization process of TS-1. On the contrary, the species of anatase-TiO₂ in some samples disappeared, and all the Ti species were in the tetra-coordination state, such as Fe-TS-1. The doping of these metals would enhance the crystallization process of zeolite. Another possibility was that these metals made use of free anatase-TiO₂ which was not involved in zeolite crystallization in bare TS-1, and combined with Ti to form another skeleton structure, such as Fe-O-Ti.

In addition, the shift of binding energy of Ti 2p electron was observed in almost all samples compared to the bare TS-1. In comparison between Mo-TS-1 and TS-1, the peak of Ti species in Mo-TS-1 shifted towards higher binding energy. Fig. 4B showed the XPS spectra of all the additional metals. As shown in the figure, the Mo⁶⁺ peak of Mo 3d_{5/2} was located at 232.42 eV. The shift of binding energies of Ti 2p and Mo 3d both proved that the electrons on TS-1 were transferred from Ti to Mo and there was a strong metal-support interaction between Mo and TS-1 zeolite. On the contrary, the peak of tetracoordination Ti species in Fe-TS-1 moved towards lower binding energy, and the Fe⁶⁺ peak of Fe 2p_{3/2}

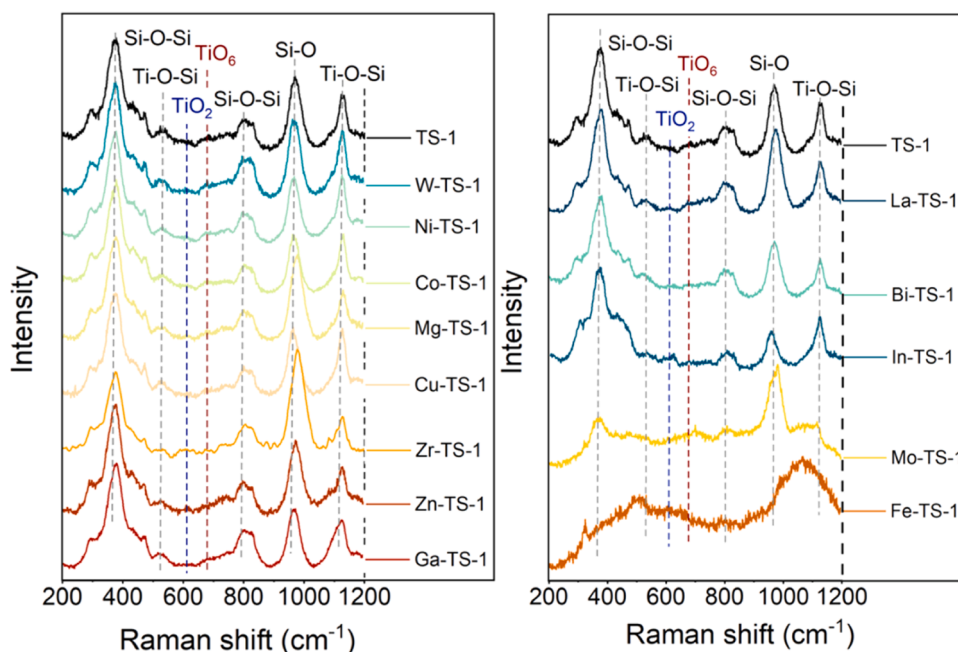


Fig. 3. UV-Raman spectra of samples with laser line of 325 nm. The Raman spectra of Al-TS-1 could not be detected due to their high fluorescence intensity.

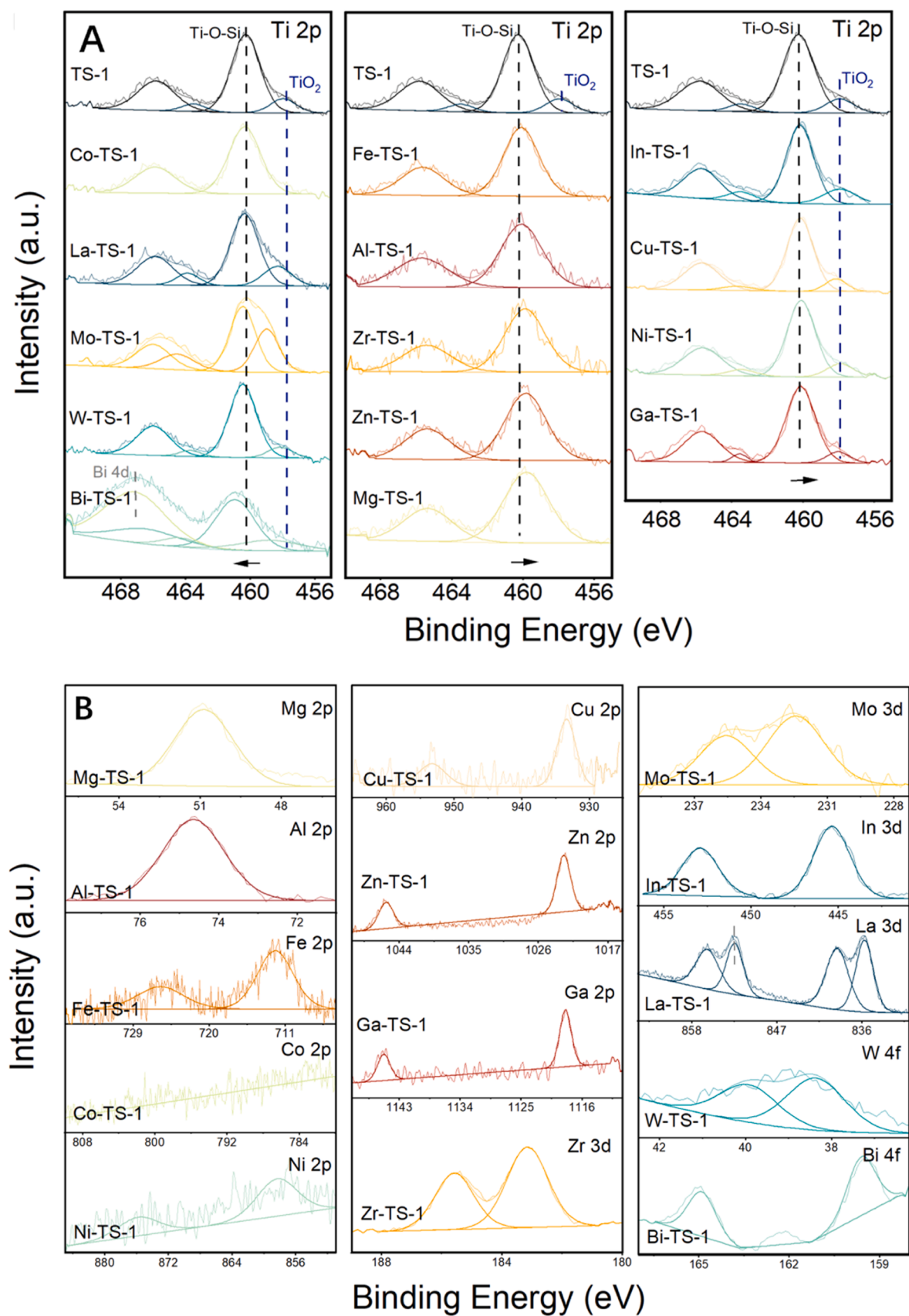


Fig. 4. XPS spectra of samples: (A) Ti 2p; (B) Additional metals.

was located at 712.16 eV, indicating that the electrons transferred from Fe to TS-1.

Combined with the above characterization and the phenomenon of the movement of the binding energy of elements, we hypothesized that the addition of various metals during the preparation process entered the zeolite through different ways. Some located in the zeolite channels to form clusters, such as Ni-TS-1; some entered the zeolite framework and replaced the T-atom (Si or Ti), generated a new skeleton structure, such as Fe-TS-1; some could not be able to enter into the zeolite due to large atomic radius or special coordination ability, but formed metal oxide layers on the surface of the zeolite, such as La-TS-1 (XPS peaks attributed to La_2O_3 species appeared in the La 3d spectrum). The electron transfer mechanism was impacted by many factors. The ionization energies of the metals concerned were listed in Table S3 [39]. The metals in the zeolite were supposed to present their most stable valence state. Then the electron ionization energy for extra electron withdrawing or donating were discussed and compared, such as third and fourth ionization energy of Fe and the fifth ionization energy of Ti. Theoretically, the third and fourth ionization energy of Fe were both lower than the fifth ionization energy of Ti. That is, electron was more likely to lose from Fe and transferred to Ti, which agreed with the result of XPS. It indicated that the electron transfer mechanism in metal-TS-1 zeolites was consistent with the law of ionization energy. Moreover, the content of each element in the sample was detected by ICP-OES, and the

results were shown in Table S4. Some metals could promote the formation of TS-1 zeolite by cocrystallization, such as Fe-TS-1; some metals could hinder the formation of Ti-O-Si framework by competitive crystallization, such as Mo-TS-1; some metals only located in the zeolite channel and had barely any effect on the zeolite synthesis, such as Ni-TS-1; while some other metals located outside the zeolite crystal and was not that stable against leaching during synthesis, such as La-TS-1.

It had been widely reported that the total acid content of the catalysts was closely related to the furfural conversion and product selectivity [16,19,24,41]. NH_3 -TPD was used to detect the acid sites of the catalysts, as shown in Fig. 5. All samples had two desorption peaks at 150 °C and 350 °C, which were corresponded to the weak acid site and strong acid site, respectively. Among them, bare TS-1 contained the least acid content, while all the other samples had a certain increase in total acid content, which could be due to the introduction of additional metals. The extra-framework metal atoms or clusters, as well as coordination saturated framework metal sites, formed Lewis acid sites. The bridged hydroxyl group adjacent to the framework non-tetravalent tetra-coordination metal offered Brønsted acid. They both increased the overall acidity of the sample [40].

The acid content of Mo-TS-1 and Zr-TS-1 were significantly increased compared with TS-1, but the acid sites were almost concentrated in the weak acid range, which was due to the fact that some metal species located in the zeolite pore and obscured the strong acid sites of the

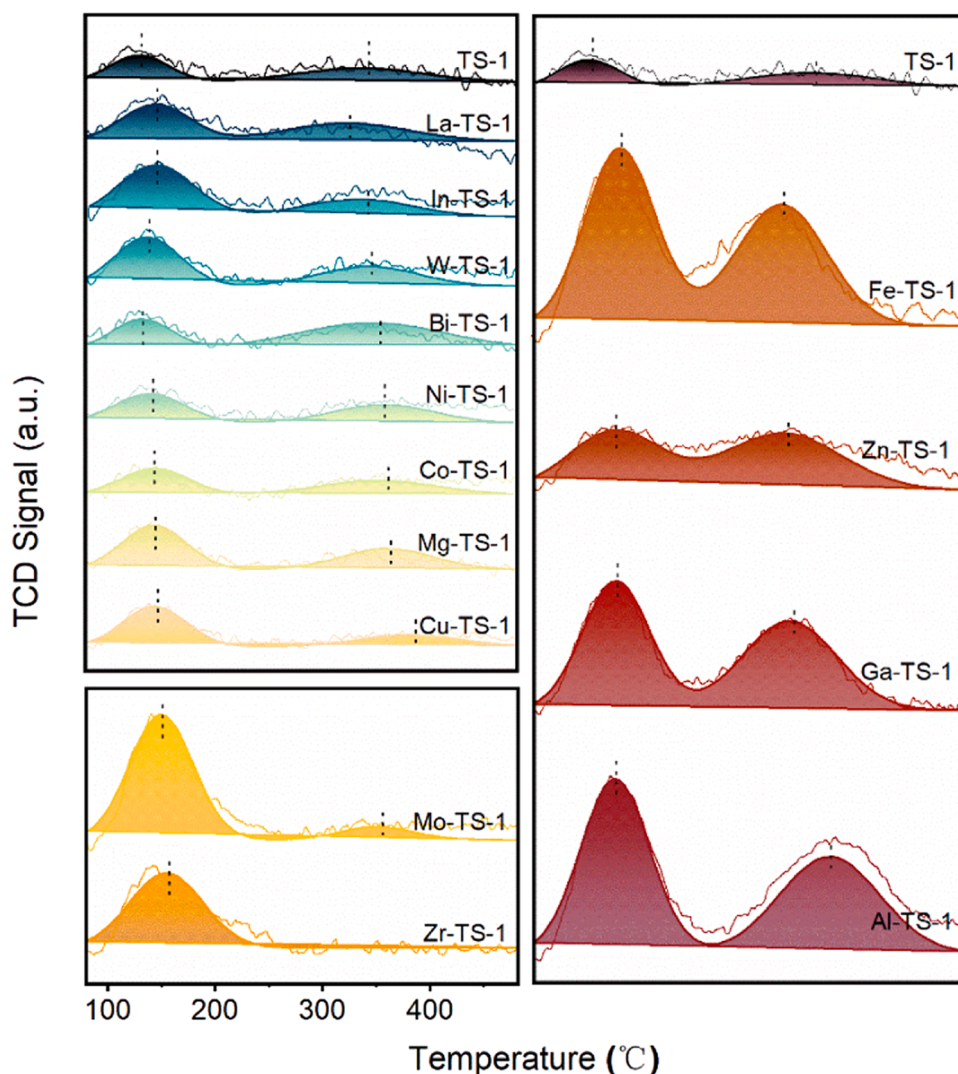


Fig. 5. NH_3 -TPD spectra of samples.

zeolite. Coincidentally, some samples such as Fe-TS-1 not only showed distinctive characteristics in morphology and pore size, but also showed both high amount of weak and strong acid sites.

Fig. 6 showed the UV-vis spectra of each sample, and the inner illustration showed the band gap width of each sample calculated by the Tauc plot method. The absorbance and band gap of most samples were similar to those of TS-1, as shown in Fig. 6A, indicating that the addition of these metals had little change in the UV response and band structure compared with TS-1. However, the properties of Fe-TS-1, In-TS-1, Bi-TS-1 and Mo-TS-1 shown in Fig. 6B were significantly different from those of TS-1. The absorbance of these samples increased significantly, indicating a stronger response to UV light. At the same time, the absorption edges of these samples were all redshifted, which meant that their band gap decreases, corresponding to the increase of the absorption range of light, as well as the utilization ability of the light source with larger wavelength was enhanced. The UV-vis spectra of these samples were analyzed, as shown in Fig. 6C. The signal generated at 210 nm was caused by the electron transfer from bonded O 2p electron to the 3d vacant orbital transition of Ti^{4+} ion, which corresponded to the existence of tetra-coordinate TiO_4 structure. The UV absorption peaks in the 310–330 nm range corresponded to anatase- TiO_2 species [42]. These results showed that In-TS-1, Bi-TS-1 and Mo-TS-1 contained more anatase- TiO_2 species than bare TS-1. In contrast, Fe-TS-1 had no obvious absorption peak in the range of 310–330 nm. Combined with the above characterization, the change of its band gap was more due to the formation of the new structure Fe-O-Ti, rather than the superposition of the absorption peak of anatase- TiO_2 .

PL was a phenomenon accompanied with the photogenerated carrier recombination process, and was intrinsically related to charge transfer

and recombination in the photocatalytic process. In order to investigate the photogenerated carrier separation efficiency of the samples and confirm the positive effect of metal modification on the photogenerated electron transfer of TS-1 zeolite, the PL spectra of the samples were compared. As shown in Fig. 7, the PL intensity of M-TS-1 modified by most metals were much lower than that of TS-1, indicating that most metals doped by our method could promote the migration of photo-generated electrons, thus inhibiting the recombination of photo-generated carriers and improving the photocatalytic activity. PL spectra of La-TS-1 had two peaks, suggesting that there were two luminescent species, which was also consistent with XPS results.

Electrochemical impedance (EIS) tests were carried out on a series of catalysts to further compare the photogenerated electron separation and utilization of samples. The results were shown in Fig. 8. The radius of the semicircular arc in the high frequency region of the EIS spectra corresponded to the resistance of charge transfer and the separation efficiency of photogenic carriers. Obviously, the radius of most metal-modified samples was smaller than that of bare TS-1, indicating that the metal and the carrier had suitable interaction, and the metal modification reduced the resistance of electron transfer and promoted the transfer of photogenerated electrons.

The band structure of a semiconductor determined its redox capacity during photocatalytic reaction. Fig. S10 showed Mottschottky (MS) curves of all samples. The MS curves of all samples had a positive slope, indicating that they belong to N-type semiconductors. The point at which the line segment of the curve intersected with the horizontal axis was the flat band potential (V_{fb}) of the sample. The flat band potential of all samples had been marked in the figure. After metal modification, the flat-band potential of all samples compared with bare TS-1 changed.

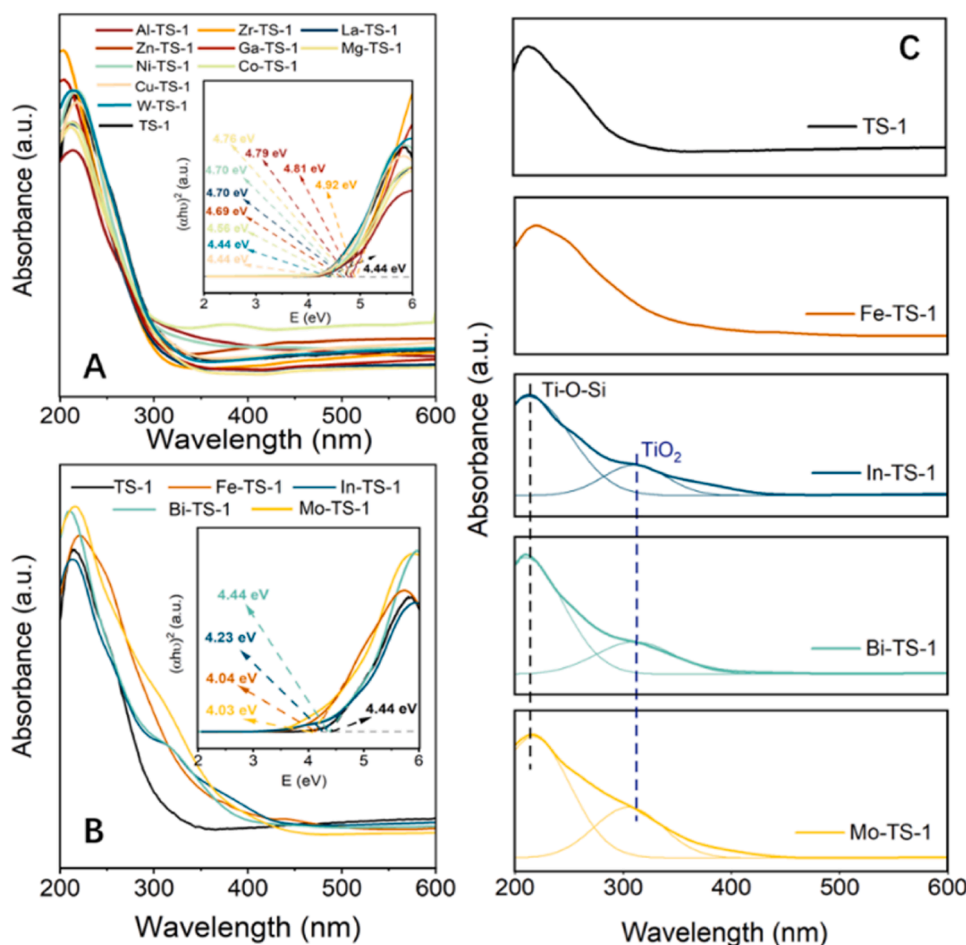


Fig. 6. UV-vis spectra of samples.

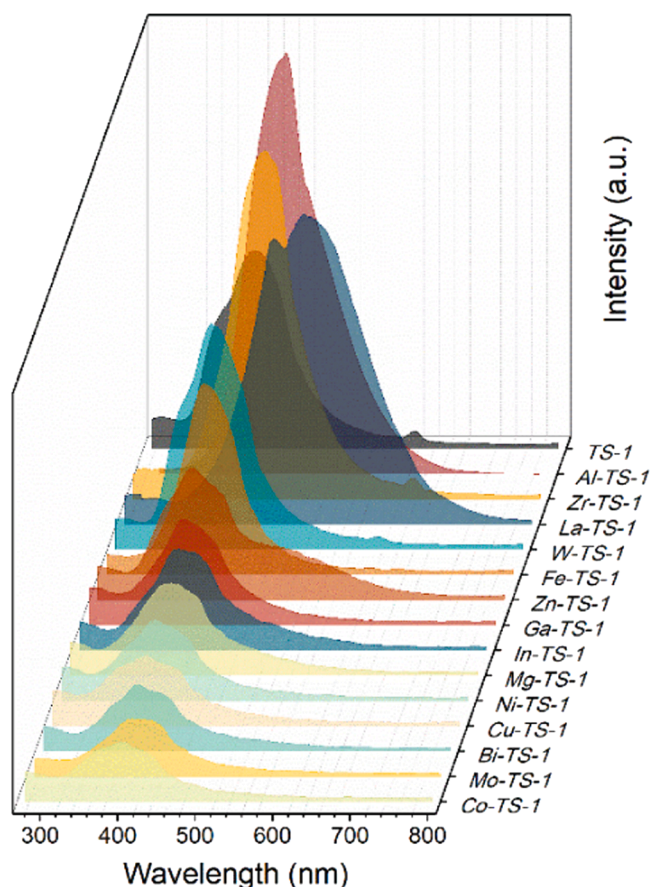


Fig. 7. PL spectra of samples under 250 nm excitation. Among them, the peak height of Al-TS-1 was reduced to 0.12 times, that of Zr-TS-1 was 0.36.

Based on the empirical formula, the conduction band potential (E_{CB}) of N-type semiconductors was usually about 0.2 eV lower than the V_{fb} , from which the E_{CB} of all samples could be calculated. The valence band potential (E_{VB}) of all samples could be further obtained from the semiconductor band gap data obtained from the UV–visible spectrum above. Energy band data of all samples were listed in Table S5.

Based on the above analysis of band structure, the migration mechanism of photogenerated carrier could be determined. The work function (ϕ) and Fermi energy level of TS-1 were measured by ultraviolet photoelectron spectroscopy (UPS), as shown in Fig. 9A. The measured secondary electron cutoff energy (E_{cutoff}) of TS-1 was 15.35 eV. The

excitation energy of He I was 21.22 eV, according to the formula: $\phi = h\nu - |E_{cutoff} - E_F|$, ϕ was calculated to be 5.87 eV [43,44]. The valence band of TS-1 had a maximum energy of 1.05 eV relative to its Fermi level. Combining the UV–vis and MS test results, the band structure of TS-1 was shown in Fig. 9B. Combined with the characterization results above, it could be inferred that different metals had different anchoring points on the carrier in the synthesized M-TS-1 catalysts. In other words, the metal would exist in the form of atoms or clusters in the zeolite channels, showing the elemental valence state; or be loaded on TS-1 in the form of oxide, as an oxidation state (such as La-TS-1); or instead of certain atoms on the zeolite skeleton, showing special valence states bonded to Si or Ti (such as Fe-TS-1 and Mo-TS-1, with metal valence between elemental and oxide). Taking Fe-TS-1 as an example, during the doping of Fe, outer electrons of Fe species would migrate to TS-1 spontaneously, and the Fermi energy level of the two species would gradually converge until reaching equilibrium. On the contrary, for Ni-TS-1, outer electrons of TS-1 would migrate to Ni species spontaneously to make the Fermi energy level reaching equilibrium. The band structure of catalyst was usually indicative of its redox capacity. Catalysts with higher valence band values had higher oxidation capacity (Ni-TS-1), while catalysts with lower valence band values had relatively controllable oxidation capacity (Fe-TS-1).

3.2. Photocatalytic reactions and structure-function relationship

These catalysts were used to catalyze furfural photo-oxidation. The reaction results were shown in Fig. 11, Fig. S5, S12 and Table S6. These results showed that all the catalysts could reach full conversion of furfural with carbon balance above 80%. The main products were maleic acid, malic acid and HFU, accompanied by a small amount of furoic acid and 5-(H)-furanone. Some of the catalytic systems with low carbon balance could be caused by the formation of formic acid from furfural over-oxidation. Using 5, 5-dimethyl-1-pyrroline N-oxide (DMPO) as the radical trapping agent, in-situ ESR was used to probe radicals generated by photo-induced activation of various reactants. When adding DMPO into the reaction system, there was an obvious specific 1:2:2:1 signal of DMPO-·OH during light irradiation. In addition, a small amount of ·O₂ was also detected, which might be generated by atmospheric O₂ on TS-1. No ·OOH was detected, as shown in Fig. 10A. Therefore, H₂O₂ participated in the reaction by forming ·OH radicals, rather than ·OOH radicals [45]. In addition, the ·O₂ produced by O₂ assisted the reaction process. After adding methanol in reaction liquid (Fig. 10B), it was found that a large number of ·OR radicals were generated, and a small amount of ·O₂ was also presented. It proved that the ·OH radical did occupy the main component of the reaction and attacked the methanol to form ·OR.

Some controlled experiments were performed to support the reaction mechanism. The furfural oxidation reaction was tested in a pure O₂

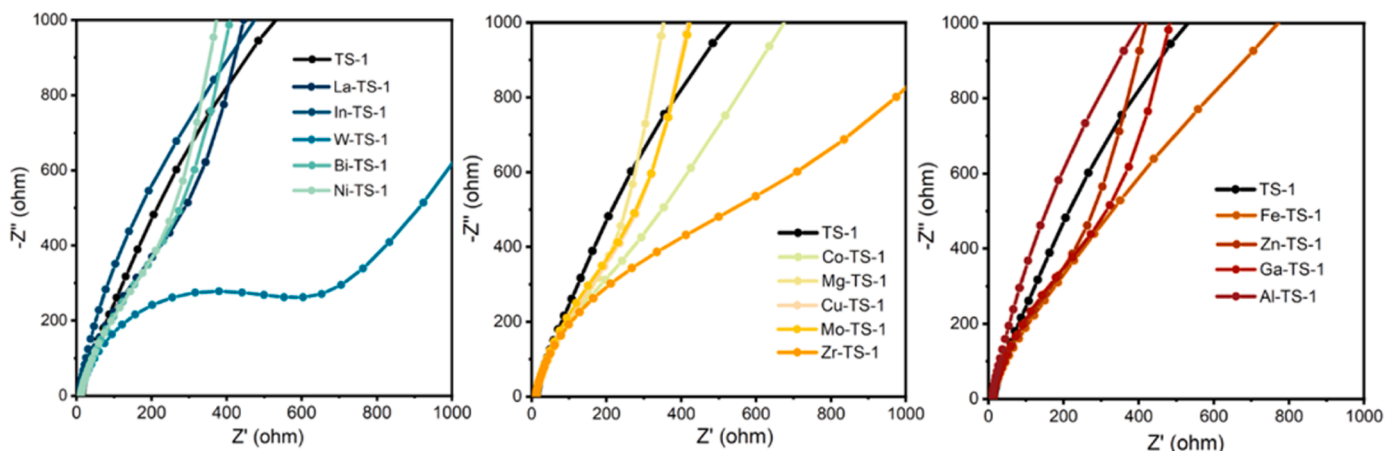


Fig. 8. EIS Nyquist plots of samples.

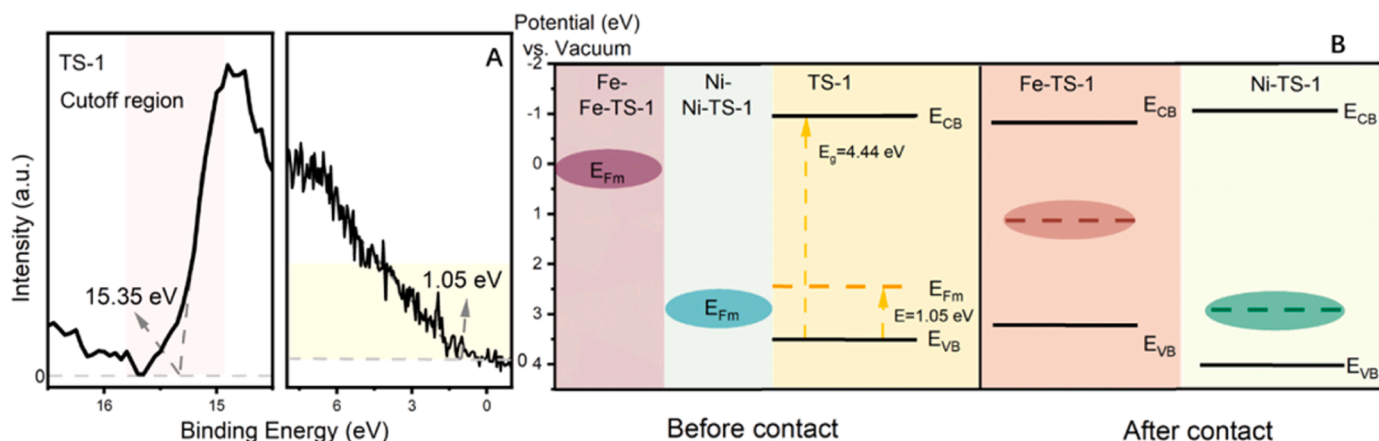


Fig. 9. (A) UPS spectra measured by He I ($h\nu = 21.22$ eV) spectra the secondary electron cutoff and E_{VB} of TS-1 with respect to the Fermi level. (B) Energy scheme before and after contact of TS-1 and Fe/Ni species.

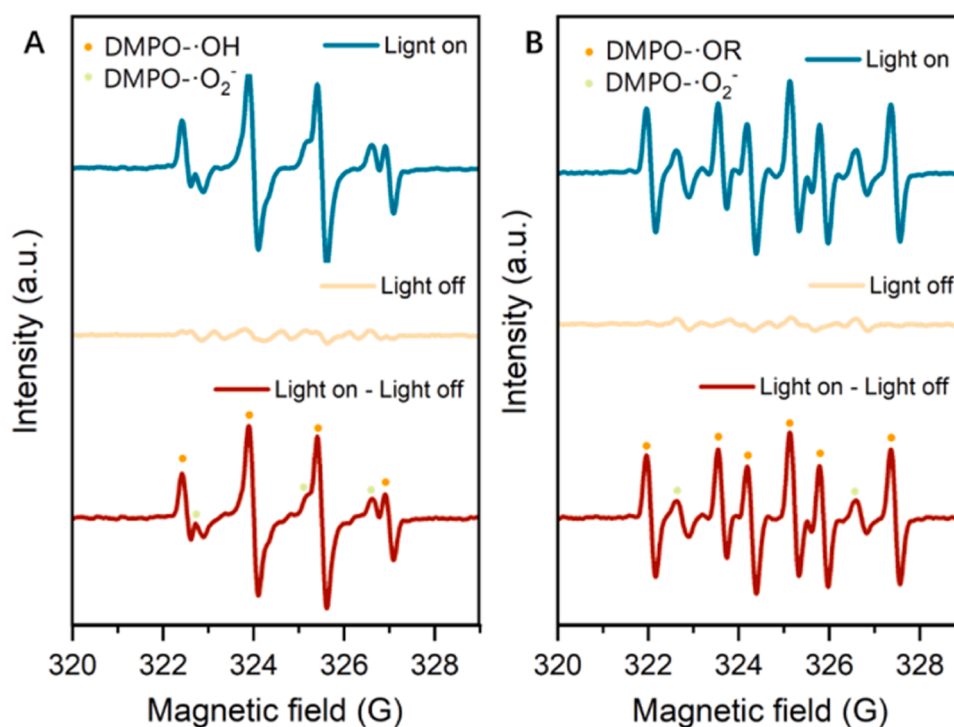


Fig. 10. In situ ESR spectra of reaction solution under UV light illumination at 298 K in the presence of DMPO over TS-1. (A) Pure water solution. (B) A mixture of water and methanol.

atmosphere and in Ar atmosphere, with other reaction conditions unchanged. It was found that in pure O₂ atmosphere, all furfural was oxidized to formic acid, and trace liquid products were detected (Table S6). Excessive \cdot O₂ would hinder the formation of maleic acid and malic acid. However, when the reaction was carried out in Ar, the oxidation process of furfural to furoic acid was inhibited obviously, and the reaction could not further proceed. It indicated that even if very little \cdot O₂ could be detected, it was necessary for the oxidation of furfural to formic acid. This further proved that in the reaction process of furfural oxidation to produce maleic acid or malic acid, H₂O₂ was as the main oxidant to form \cdot OH radical for the reaction, while the appropriate amount of \cdot O₂ would assist in the oxidation of furfural to furoic acid. Based on the above discussions, the catalytic mechanism can be proposed as schematically illustrated in Scheme 3. When exposed to light, the photogenerated electrons e^- on the conduction band of M-TS-1 induced H₂O₂ to form \cdot OH radicals and O₂ to \cdot O₂. Subsequently, in the

presence of \cdot O₂ as an oxidizing agent, furfural was converted to furoic acid on the valence band of M-TS-1, and carboxylic acid group was removed to form the C4 product 5-(H)-furanone, accompanied by the formation of equivalent formic acid. Furoic acid and furanone were both intermediate products that could be detected, which was formed via the Baeyer-Villiger oxidation pathway [24]. Subsequently, 5-(H)-furanone was further oxidized to HFU with the oxidizing agent \cdot OH, and then the ring was opened to obtain maleic acid. Interestingly, under our catalytic conditions, the synergistic effect of light and TS-1 series catalysts could further hydrate and oxidize maleic acid to malic acid in aqueous solution system, which has not been reported before.

Furthermore, there were significant differences in product selectivity over different catalysts. On this basis, the relationship between product distribution and physicochemical properties of catalyst was studied. Fig. 12 listed the physical and chemical characteristics of the catalysts measured in the catalyst characterization mentioned above, including

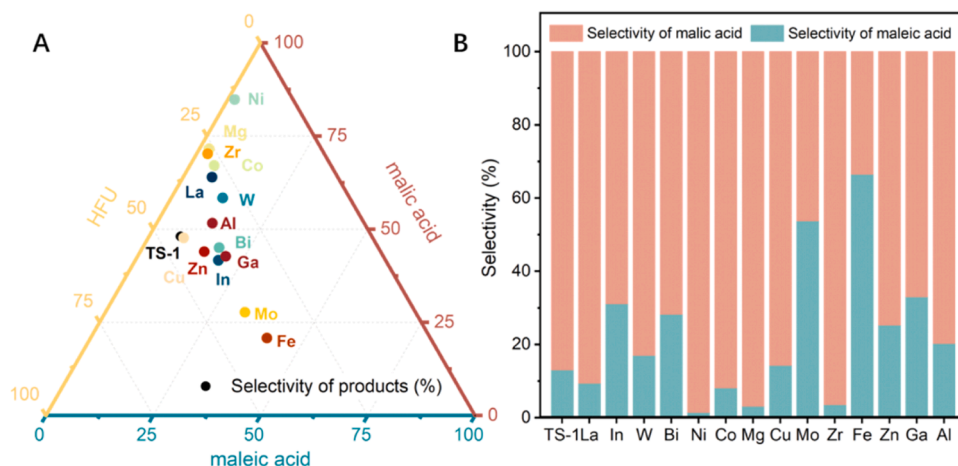
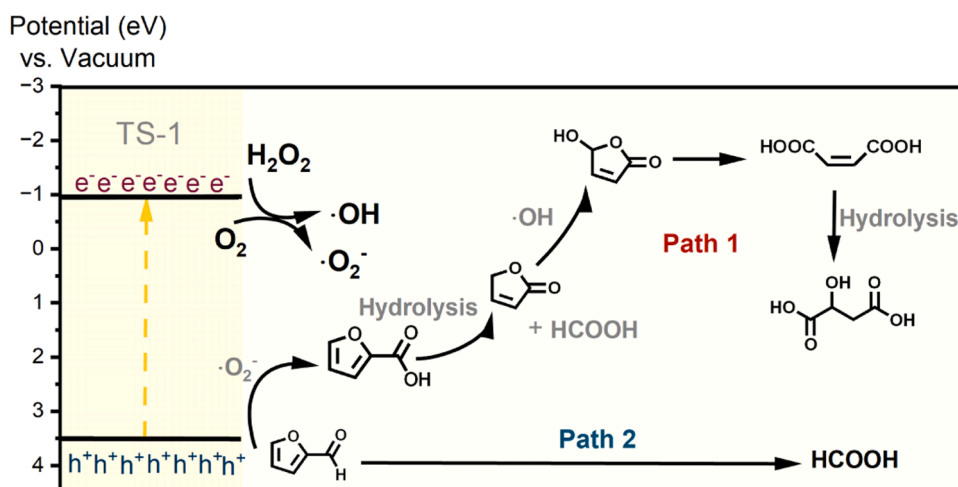


Fig. 11. Selectivity of products on different catalysts ((A) only HFU, maleic acid and malic acid were considered; (B) only maleic acid and malic acid were considered). Reaction conditions: 0.1 mmol furfural, 5 mg of the catalyst, 0.6 mmol 15% H_2O_2 solution, irradiation wavelength 390 nm, 25 °C, 10 h.



Scheme 3. Formation Pathway of Malic acid from furfural.

the grain size by XRD, the specific surface area, pore volume and pore size by N_2 adsorption-desorption, the content ratio of Ti and Si on the catalyst surface and the content of different species of Ti by XPS, the amount of catalyst acid by NH_3 -TPD and the band structure of catalyst by MS. The correlation between these properties and the selectivity of maleic acid and malic acid was explored. Obviously, the selectivity of the product was positively related to the grain size, pore volume, pore size, acid content and band structure of the catalyst. It indicated that these factors together led to the different distribution of the product.

Based on the above results, it indicated that the doping of different metal would obviously impact the physiochemical properties of TS-1 zeolite and thus varying the selectivity. Firstly, some metals that was tended to replace the T-atom and located in zeolite framework, such as Fe and Mo, would be beneficial for the selectively yield of maleic acid. The doping of these metals into zeolite will lead to the distortion of zeolite framework and therefore decreased the volume and size of zeolite micropore. It will resist the further adsorption, desorption and mass transfer of intermediates and products, and will shape-selectively hinder the formation of larger molecular, malic acid. Secondly, the acidity of the catalyst was the key factor that influenced the product distribution. Moderate acidity was beneficial for the formation of malic acid. Acid sites could catalyze the formation of maleic acid [19] and further hydration of maleic acid to malic acid. In this metal-TS-1 photocatalytic system, the weak acid sites could promote the formation of

maleic acid; while moderate acidity could lead to further hydration to malic acid. Thirdly, the band structure of photocatalyst strongly affected the product distribution. Higher E_{VB} meant stronger oxidation capacity of the catalyst, which was consistent with the results of the reactions. The band structure of the catalyst changed with the doping of metal. The valence band of Fe-TS-1 decreased significantly, and that of Ni-TS-1 increased significantly. It led to the highest selectivity of maleic acid and malic acid over Fe-TS-1 and Ni-TS-1, respectively.

Over these metal-TS-1 catalysts, the yield of maleic acid reached as high as 40% over Fe-TS-1. Meanwhile, the yield of malic acid reached as high as 63% over Ni-TS-1. Moreover, as shown in Fig. S13, the catalysts had good stability. Using TS-1 as a reference, both Fe-TS-1, in which we considered Fe entered the skeleton to participate in the zeolite structure, and Ni-TS-1, which Ni only entered the zeolite pore without changing the zeolite structure, all had good activity after five cycles. Among them, Fe-TS-1 had better stability than Ni-TS-1, which might be because the metal anchored to the framework was less susceptible to loss than the metal particles in the pore. Although selective production of single products could hardly be achieved in this catalytic system at present, nor could the residue of intermediate HFU be avoided, the effective photocatalytic production of malic acid was achieved for the first time. Based on the above discussion and consideration of catalytic system, different metals could be doped into TS-1 zeolite appropriately. Meanwhile, we believed that the doping of metal was an effective procedure to adjust



Fig. 12. Heat map of correlation analysis between product selectivity and catalyst physicochemical properties.

the structure and physicochemical properties of zeolite. Matel-TS-1 was also expected to be widely used in photocatalytic system to achieve more selective reactions.

4. Conclusion

A series of Metal-TS-1 zeolite catalysts was synthesized and applied in the photocatalytic oxidation of furfural. Selective preparation of downstream C_4 carboxylic acid derivatives was realized. Maleic acid, malic acid, and 5-hydroxy-2,5(H)-furanone was directly prepared from furfural by photocatalysis at ambient temperature and pressure. The synergistic effect of pore structure, acidity and energy band structure of catalysts affected the product distribution. Smaller pore size would prevent the further conversion of maleic acid to malic acid; moderate acidity was beneficial for the preparation of malic acid; lower valence band was in favor of maleic acid production while higher valence band was tended to form malic acid. The yield of maleic acid reached as high as 40% over Fe-TS-1, meanwhile, the yield of malic acid reached as high as 63% over Ni-TS-1. Based on this study, the doping of metal was believed to be an effective procedure to adjust the structure and physicochemical properties of zeolite. The key step of metal incorporation into zeolite brings a potential strategy for the design and synthesis of heteroatomic zeolite photocatalysts. Matel-TS-1 was also expected to be widely used in photocatalytic system to achieve more selective reactions.

CRedit authorship contribution statement

Wanying Liang: Methodology, Validation, Formal analysis, Investigation, Writing – original draft, Visualization. **Guangyue Xu:** Conceptualization, Resources, Writing – review & editing, Visualization, Project administration, Funding acquisition. **Yao Fu:** Resources, Supervision, Funding acquisition.

Declaration of Competing Interest

There are no conflicts to declare.

Data availability

No data was used for the research described in the article.

Acknowledgements

This work was supported by the National Natural Science Foundation of China (22293011, 51821006, 21905266), the Institute of Energy, Hefei Comprehensive National Science Center under Grant No. 21KZS219, and the Fundamental Research Funds for the Central Universities (20720220007, WK3530000013).

Appendix A. Supporting information

Supplementary data associated with this article can be found in the online version at [doi:10.1016/j.apcatb.2023.123220](https://doi.org/10.1016/j.apcatb.2023.123220).

References

- [1] R. Bosch, M. Pol, J. Philp, Policy: define biomass sustainability, *Nature* 523 (2015) 526–527.
- [2] J. Martinez, Chemistry 2030: a roadmap for a new decade, *Angew. Chem. Int. Ed.* 60 (2021) 4956–4960.
- [3] C. Wang, X. Zhang, Q. Liu, Q. Zhang, L. Chen, L. Ma, A review of conversion of lignocellulose biomass to liquid transport fuels by integrated refining strategies, *Fuel Process. Technol.* 208 (2020), 106485.
- [4] M. Sajid, U. Farooq, G. Bary, M. Azime, X. Zhao, Sustainable production of levulinic acid and its derivatives for fuel additives and chemicals: progress, challenges, and prospects, *Green. Chem.* 23 (2021) 9198–9238.
- [5] K. Alper, K. Tekin, S. Karagöz, A. Ragauskas, Sustainable energy and fuels from biomass: a review focusing on hydrothermal biomass processing, *Sustain. Energ. Fuels.* 4 (2020) 4390–4414.
- [6] M. Antar, D. Lyu, M. Nazari, A. Shah, X. Zhou, D. Smith, Biomass for a sustainable bioeconomy: an overview of world biomass production and utilization, *Renew. Sust. Energ. Rev.* 139 (2021) 110691–110708.

- [7] B. Stadler, C. Wulf, T. Werner, S. Tin, J. Vries, Catalytic approaches to monomers for polymers based on renewables, *ACS Catal.* 9 (2019) 8012–8067.
- [8] M. Musolino, M. Molina, R. Tost, F. Aricò, Purolite-catalyzed etherification of 2,5-Bis(hydroxymethyl)furan: a systematic study, *ACS Sustain. Chem. Eng.* 7 (2019) 10221–10226.
- [9] J. Bozell, G. Petersen, Technology development for the production of biobased products from biorefinery carbohydrates—the US Department of Energy's "Top 10" revisited, *Green. Chem.* 12 (2010) 539–554.
- [10] R. Mariscal, P. Maireles-Torres, M. Ojeda, I. Sádaba, M. Granados, *Energy Environ. Sci.* 9 (2016) 1144–1189.
- [11] S. Albonetti, F. Cavani, F. Trifiro, Key aspects of catalyst design for the selective oxidation of paraffins, *Catal. Rev.: Sci. Eng.* 38 (1996) 413–438.
- [12] X. Li, B. Ho, D. Lima, Y. Zhang, Highly efficient formic acid-mediated oxidation of renewable furfural to maleic acid with H_2O_2 , *Green. Chem.* 19 (2017) 914–918.
- [13] X. Zhao, X. Kong, F. Wang, R. Fang, Y. Li, Metal sub-nanoclusters confined within hierarchical porous carbons with high oxidation activity, *Angew. Chem., Int. Ed.* 60 (2021) 10842–10849.
- [14] T. Soták, M. Hronec, M. Gál, E. Dobročka, J. Škriniarová, Aqueous-phase oxidation of furfural to maleic acid catalyzed by copper phosphate catalysts, *Catal. Lett.* 147 (2012) 2714–2723.
- [15] X. Li, X. Lan, T. Wang, Selective oxidation of furfural in a bi-phasic system with homogeneous acid, *Catal. Catal. Today* 276 (2016) 97–104.
- [16] C. Nguyen, J. Boo, C. Liu, T. Ahamad, S. Alshehri, B. Matsagar, K. Wu, Oxidation of biomass-derived furans to maleic acid over nitrogen-doped carbon catalysts under acid-free conditions, *Catal. Sci. Technol.* 10 (2020) 1498–1506.
- [17] N. Fagúndez, I. Telleria, P. Arias, J. Fierro, R. Mariscal, M. Granados, Aqueous-phase catalytic oxidation of furfural with H_2O_2 : high yield of maleic acid by using titanium silicalite-1, *RSC Adv.* 4 (2014) 54960–54972.
- [18] Y. Lou, S. Marinkovic, B. Estrine, W. Qiang, G. Enderlin, Oxidation of furfural and furan derivatives to maleic acid in the presence of a simple catalyst system based on acetic acid and TS-1 and hydrogen peroxide, *ACS Omega* 5 (2020) 2561–2568.
- [19] H. Zhang, S. Wang, H. Zhang, J. Clark, F. Cao, A biomass-derived metal-free catalyst doped with phosphorus for highly efficient and selective oxidation of furfural into maleic acid, *Green. Chem.* 23 (2021) 1370–1381.
- [20] T. Yang, W. Li, Q. Liu, M. Su, T. Zhang, J. Ma, Synthesis of maleic acid from biomass-derived furfural in the presence of KBr/graphitic carbon nitride (g-C₃N₄) catalyst and hydrogen peroxide, *Biores* 14 (2019) 5025–5044.
- [21] H. Choudhary, S. Nishimura, K. Ebitani, Metal-free oxidative synthesis of succinic acid from biomass-derived furan compounds using a solid acid catalyst with hydrogen peroxide, *Appl. Catal., A* 458 (2013) 55–62.
- [22] Y. Peng, L. Qian, J. Ding, T. Zheng, Y. Zhang, B. Li, Syntheses, structures and photocatalytic degradation of organic dyes for two isostructural copper coordination polymers involving in situ hydroxylation reaction, *J. Coord. Chem.* 71 (2018) 1392–1402.
- [23] J. Song, B. Wang, H. Hu, L. Gou, Q. Wu, X. Yang, Y. Shangguan, F. Dong, G. Xue, In situ hydrothermal syntheses, crystal structures and luminescent properties of two novel zinc (II) coordination polymers based on tetrapyridyl ligand, *Inorg. Chim. Acta* 366 (2011) 134–140.
- [24] Y. Palai, A. Shrotri, A. Fukuoka, Selective oxidation of furfural to succinic acid over lewis acidic Sn-beta, *ACS Catal.* 12 (2022) 3534–3542.
- [25] V. Kotzabasakis, G. Vassilikogiannakis, M. Stratakis, Total synthesis and structural revision of (+)-yaoshanenolide B, *Org. Lett.* 18 (2016) 4982–4985.
- [26] S. Thorat, M. Palange, R. Kontham, Four-step total synthesis of (+)-yaoshanenolides A and B, *ACS Omega* 3 (2018) 7036–7045.
- [27] L. Badovskaya, V. Poskonin, L. Povarova, Synthesis of functional furan derivatives by oxidation of furans and formylfurans with hydrogen peroxide, *Russ. Chem. B* 66 (2017) 593–599.
- [28] J. Hermens, A. Jansma, B. Feringa, Highly efficient biobased synthesis of acrylic acid, *Angew. Chem., Int. Ed.* 61 (2022), e202112618.
- [29] M. Oikawa, Y. Sugeno, H. Takeda, Y. Takasaki, S. Takamizawa, R. Irie, Four stereoisomers of 2-aminomethyl-1-cyclopropanecarboxylic acid: synthesis and biological evaluation, *B. Chem. Soc. Jpn.* 92 (2019) 1816–1823.
- [30] B. Chen, F. Li, G. Yuan, Selective hydrodeoxygenation of 5-hydroxy-2(5H)-furanone to γ -butyrolactone over Pt/mesoporous solid acid bifunctional catalyst, *RSC Adv.* 7 (2017) 21145–21152.
- [31] Q. Wu, H. Wang, Y. Jia, G. Zhou, Kinetics of the acid orange 7 degradation in the photocatalytic system of UV/ H_2O_2 /TS-1, *J. Water Process Eng.* 19 (2017) 106–111.
- [32] N. Li, B. Yang, M. Liu, Y. Chen, J. Zhou, Synergetic photo-epoxidation of propylene with molecular oxygen over bimetallic Au–Ag/TS-1 photocatalysts, *Chinese, J. Catal.* 38 (2017) 831–843.
- [33] X. Zhang, Z. Jin, Y. Li, S. Li, G. Lu, Photocatalytic hydrogen generation over Eosin Y-Sensitized TS-1 zeolite, *Appl. Surf. Sci.* 254 (2008), 4452–2256.
- [34] Y. Sun, G. Li, Y. Gong, Z. Sun, H. Yao, X. Zhou, Ag and TiO_2 nanoparticles co-modified defective zeolite TS-1 for improved photocatalytic CO_2 reduction, *J. Hazard. Mater.* 403 (2021), 124019.
- [35] Q. Zhang, S. Gao, J. Yu, Metal sites in zeolites: synthesis, characterization, and catalysis, *Chem. Rev.* (2022).
- [36] D. Serrano, R. Sanz, P. Pizarro, I. Moreno, Turning TS-1 zeolite into a highly active catalyst for olefin epoxidation with organic hydroperoxides, *Chem. Commun.* 11 (2009) 1407–1409.
- [37] G. Tozzola, M. Mantegazza, G. Ranghino, G. Petrini, S. Bordiga, G. Ricchiardi, C. Lamberti, R. Zulian, A. Zecchina, On the structure of the active site of Ti-silicalite in reactions with hydrogen peroxide: a vibrational and computational study, *J. Catal.* 179 (1998) 64–71.
- [38] E. Jorda, A. Tuel, R. Teissier, J. Kervennal, TiF₄: An original and very interesting precursor to the synthesis of titanium containing silicalite-1, *Zeolites* 19 (1997) 238–245.
- [39] C. Moore, National Standard Reference Data Series 34, U.S. Government Printing office, Washington, D.C., 1970.
- [40] M. Ravi, V. Sushkevich, J. Bokhoven, Towards a better understanding of Lewis acidic aluminium in zeolites, *Nat. Mater.* 19 (2020) 1047–1056.
- [41] P. Malibo, P. Makgwane, Heterostructured redox-active V_2O_5/SnO_2 oxide nanocatalyst for aqueous-phase oxidation of furfural to renewable maleic acid, *ChemistrySelect* 5 (2020) 6255–6267.
- [42] W. Xu, T. Zhang, R. Bai, P. Zhang, J. Yu, A one-step rapid synthesis of TS-1 zeolites with highly catalytically active mononuclear TiO_6 species, *J. Mater. Chem. A* 8 (2020) 9677–9683.
- [43] J. Li, Z. Li, X. Liu, C. Li, Y. Zheng, K. Yeung, Z. Cui, Y. Liang, S. Zhu, W. Hu, Y. Qi, T. Zhang, X. Wang, S. Wu, *Nat. Commun.* 12 (2021) 1224.
- [44] H. Cheng, J. Wang, Y. Yang, H. Shi, J. Shi, X. Jiao, P. Han, X. Yao, W. Chen, X. Wei, P. Chu, X. Zhang, Ti_3C_2TX MXene modified with ZnTCPP with bacteria capturing capability and enhanced visible light photocatalytic antibacterial activity, *Small* 18 (2022), 2200857.
- [45] X. Sun, X. Chen, C. Fu, Q. Yu, X. Zheng, F. Fang, Y. Liu, J. Zhu, W. Zhang, W. Huang, Molecular oxygen enhances H_2O_2 utilization for the photocatalytic conversion of methane to liquid-phase oxygenates, *Nat. Commun.* 13 (2022) 6677.